JOURNAL OF Applied Polymer SCIENCE

Nylon 66 Nanofibers Prepared by CO_2 Laser Supersonic Drawing

Akihiro Suzuki, Takumi Mikuni, Toshinori Hasegawa
Interdisciplinary Graduate School of Medicine and Engineering, University of Yamanashi, Kofu 400-8511, Japan
Correspondence to: A. Suzuki (E-mail: a-suzuki@yamanashi.ac.jp)

ABSTRACT: Nylon 66 nanofibers were prepared by irradiating as-spun nylon 66 fibers with radiation from a carbon dioxide (CO_2) laser while drawing them at supersonic velocities. A supersonic jet was generated by blowing air into a vacuum chamber through the fiber injection orifice. The fiber diameter depended on the drawing conditions used, such as laser power, chamber pressure, laser irradiation point, and fiber supply speed. A nanofiber obtained at a laser power of 20 W and a chamber pressure of 20 kPa had an average diameter of 0.337 μm and a draw ratio of 291,664, and the drawing speed in the CO_2 laser supersonic drawing was 486 m s^{-1}. The nanofibers showed two melting peaks at about 257 and 272°C. The lower melting peak is observed at the same temperature as that of the as-spun fiber, whereas the higher melting peak is about 15°C higher than the lower one. © 2013 Wiley Periodicals, Inc. J. Appl. Polym. Sci. **2014**, *131*, 40015.

KEYWORDS: fibers; properties and characterization; polyamides

Received 6 August 2013; accepted 27 September 2013
DOI: 10.1002/app.40015

INTRODUCTION

Nanofibers are used in a variety of applications, such as membranes,[1–3] biomedical devices,[4] and scaffolds for tissue engineering.[5–9] Nanofibers have been produced by electrospinning,[10–18] melt electrospinning,[19–21] sea-island-type conjugated melt spinning, single-orifice melt blowing,[22] and jet blowing.[23] Among these methods, electrospinning is most widely used for preparing nanofibers. Although electrospinning is used to fabricate various nanofibers, it cannot be applied to polymers that are insoluble in solvents, such as polyolefins and fluoropolymers. In addition, considering solvent toxicity and environmental safety, solution electrospinning is not an appropriate technique for the mass production of nanofibers.

We propose CO_2 laser supersonic drawing (CLSD) as a technique to easily prepare nanofibers, because it uses only CO_2 laser irradiation and does not require any additional processes or solvents. CLSD prevents scattering of the nanofibers in air, because it is performed under vacuum. This closed system technique also offers superior environmental safety compared to electrospinning and melt blowing, which are carried out in open systems. Nanofibers obtained by CLSD can be made indefinitely long, because the fiber is supplied at a constant speed and is continuously irradiated with a laser beam. CLSD has already been applied for the production of poly(L-lactic acid) (PLLA),[24] polyethylene terephthalate (PET),[25] poly(ethylene-2, 6-naphthalate),[26] poly(glycolic acid),[27] isotactic polypropylene (iPP),[28] poly(tetrafluoroethylene-*co*-perfluoropropyl vinyl ether),[29] and ethylene tetrafluoroethylene[30] nanofibers, and all of these nanofibers were obtained without using any solvent or without removing the second component.In this study, the nylon 66 (N66) fiber was drawn by CLSD at various conditions, and the drawing conditions to form the nanofibers were investigated. N66 nanofibers were also prepared by electrospinning using a solution of N66–formic acid onto a metallic collector under high voltage, and the average fiber diameter in this case was 0.550 μm.[31] Here, we present results pertaining to the relationship between the morphology of the nanofibers, the superstructure, and the drawing conditions.

EXPERIMENTAL

Original fibers were produced from commercial grade N66 pellets using a laboratory-scale melt extruder and take-up unit. The original fibers were spun into monofilaments at a spinning temperature of 285°C. The as-spun N66 fibers had a diameter of 182 μm and were found to be isotropic, from wide-angle X-ray diffraction (WAXD) patterns. The number- and weight-average molecular weights of the as-spun N66 fibers were 8300 and 34,100, respectively.

The morphology of the produced nanofibers was determined by scanning electron microscopy (SEM; JSM-6060LV, JEOL, Japan) using an accelerating voltage of 10 kV. Before the SEM observations, the samples were coated with platinum using a sputter coater. The average diameter and diameter distribution of the nanofibers were measured using an imaging analyzer. The average diameter of a fiber was determined by averaging the diameters measured at 100 locations in a webbed fiber.

The necking of the fiber formed by laser heating during the supersonic drawing process was recorded using a high-speed camera (Motion Analysis Microscope VW-6000, Keyence) equipped with a long-range zoom lens (VH-Z50L/W, Keyence). The high-speed camera is capable of high-speed recording of up to 24,000 frames·s^{-1}, and the zoom lens achieved an 85 mm viewing distance at a maximum 500× magnification.

Differential scanning calorimetry (DSC) measurements were conducted using a calorimeter (Therm Plus 2 DSC 8230C; Rigaku Co., Japan). The DSC scans were performed within the temperature range of 25–290°C at a heating rate of 10°C·min^{-1}. All DSC experiments were carried out under a nitrogen purge. The DSC instrument was calibrated using indium. The degree of crystallinity (X_c) was determined from the heat of fusion (ΔH_m) using the following expression:

$$X_c = \frac{\Delta H_m}{-192} \times 100 \quad (1)$$

where -192 J·g^{-1} is used as the heat of fusion of the crystalline phase of N66.[32]

Infrared spectroscopy measurements were performed using a Fourier-transform infrared (FT-IR) spectrometer (FT/IR 4200, JASCO Co.) with a resolution of 4 cm^{-1}. Each spectrum was obtained from 80 scans.

WAXD patterns of the nanofibers were obtained using an imaging-plate (IP) film and an IP detector (R-AXIS DS3C; Rigaku Co.). The IP film was attached to an X-ray generator (Rigaku Co.) operated at 40 kV and 200 mA. The radiation used was Ni-filtered Cu K_α. The sample-to-film distance was 40 mm. The fiber was exposed for 60 min to the X-ray beam from a 0.4-mm diameter pinhole collimator. The degree of crystal orientation (π) estimated from the half-width (H) of the meridian reflection peak. The π value was estimated from WAXD pattern measured by the IP through the software for analyzing data.

The π value is given by the equation:

$$\pi = \frac{180 - H}{180} \quad (2)$$

Figure 1 shows the apparatus used for CLSD. It consists of a spool to supply the fiber, a continuous-wave CO_2 laser with an output wavelength of 10.6 μm and a maximum power of 40 W, an acrylic vacuum chamber with Zn–Se windows and a 0.5-mm diameter orifice for injecting the fiber, a power meter, a movable platen, the high-speed camera equipped a long-range zoom lens, and a vacuum pump. Observation in the vacuum chamber is possible through a viewing window with the zoom lens on the outside. The vacuum chamber was placed on the movable platen that consists of a microalignment stage and a laboratory jack that can be moved parallel to the Y- and Z-axes allowing the laser irradiation point on the fiber to be finely adjusted.

RESULTS AND DISCUSSION

When performing CLSD, it is very important to determine the drawing conditions, such as laser irradiation position, chamber pressure, laser power, and fiber supply speed. The drawing condition dominates the morphology and characteristics of the drawn fiber. It will be very useful to understand the mechanism of the CLSD process if the relationship between the drawing condition, its morphology and characteristics of the drawn fiber can be elucidated.

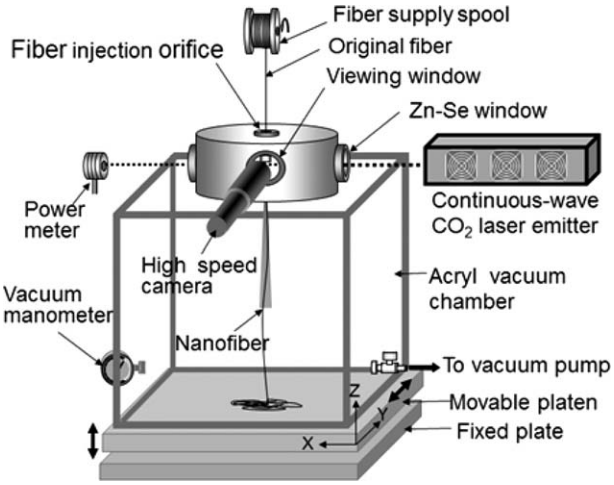

Figure 1. Schematic diagram of the apparatus used for CO_2-laser supersonic drawing.

Laser Irradiation Position and Chamber Pressure Dependence of Fiber Diameter and Its Superstructure

It is very important to investigate the laser irradiation position because the drawing force and laser power depend strongly on the distance from the orifice. To clarify this effect on the fiber diameter and superstructure, CLSD was carried out by varying the laser irradiation position and chamber pressure.

Figure 2 shows a schematic diagram of the relative positions of the orifice and laser beam to explain the laser irradiation position, and the flow velocity distribution of the air jet in the XZ-plane calculated by a three-dimensional finite element method.[28] First, the laser beam was operated at $P_L = \alpha W$ without shading by the orifice attached to the vacuum chamber as shown in Figure 2(a). Next, the vacuum chamber was lowered using the laboratory jack in the Z-axis direction. When the laser beam operating at $P_L = \alpha W$ was just reduced to half ($P_L = \alpha/2W$) by the orifice, the displacement was set to $D = 0$ mm [see Figure 2(b)], where the beam top and outlet of the orifice are in agreement. The intensity of the beam top at $D = 0$ mm is the highest laser power because the CO_2 laser beam is a Gaussian beam. The laser power at the outlet of the orifice decreases as the D value increases.

Figure 3 shows the dependence of the average fiber diameter (d_{av}) at five different chamber pressures (p_{ch}) on various displacements (D) between the beam top and the outlet of the orifice in the Z direction. The laser power and fiber supply speed were kept constant at 10 W and 0.1 m min^{-1}, respectively, during the series of experiments. As the displacement was increased, the fiber diameter initially decreased and then increased after attaining a minimum diameter at $D = 2$ mm at

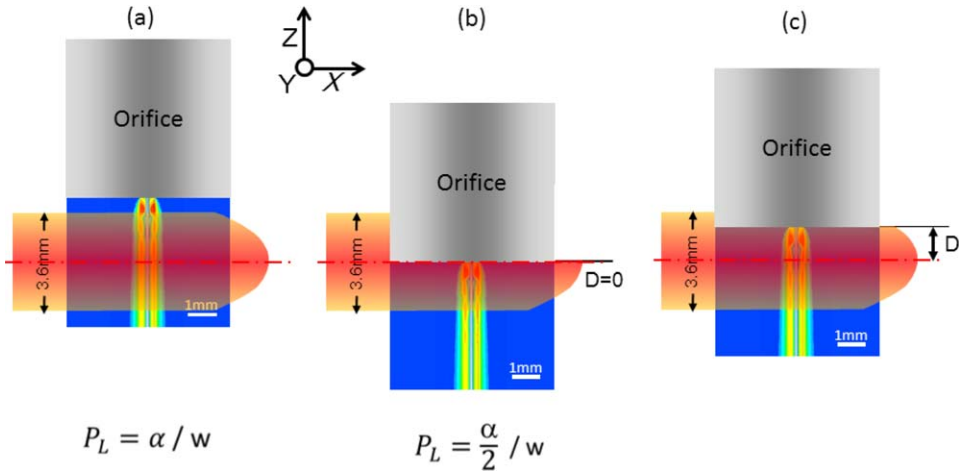

Figure 2. Schematic diagram of the relative position between the orifice and laser beam to explain the laser irradiation position, and the flow velocity distribution of the air jet in the *XZ*-plane calculated by a three-dimensional finite element method. [Color figure can be viewed in the online issue, which is available at wileyonlinelibrary.com.]

each chamber pressure. For each displacement, the average fiber diameter decreased as the chamber pressure decreased, and the thinnest nanofiber was obtained at $p_{ch} = 10$ kPa, with a diameter of 0.488 μm. The fiber does not become thinner because the drag force in the air jet decreases as the laser irradiation point is separated from the outlet of the orifice.

Figure 4 shows scanning electron micrographs of the fibers drawn at various chamber pressures and displacements, as well as photographs (500×) indicating the necking formed by laser heating during the supersonic drawing process. The photographs were taken perpendicular to the axis of the laser beam using a high-speed camera equipped the long range zoom lens as described earlier. The fiber was irradiated with the laser from the left side as shown in the photographs. In all fibers, except for the fibers drawn at $D = 0$ mm at $p_{ch} = 10$ and 20 kPa, necking was stably formed by laser heating. Because the fibers drawn at $D = 0$ mm at $p_{ch} = 10$ and 20 kPa

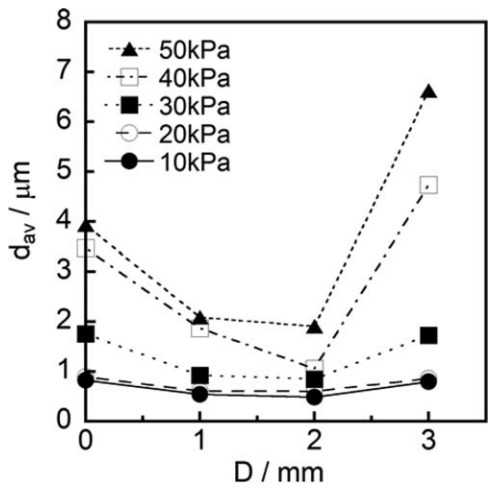

Figure 3. Dependence of the average fiber diameter at five different chamber pressures (p_{ch}) on various displacements (D) between the beam top and the outlet of the orifice in the Z direction.

are strongly heated by irradiating the beam top at the outlet of the orifice in the supersonic jet, its melt viscosity decreases rapidly, and the melted fiber is blown off under the supersonic jet without forming the neck. However, the melted fiber forms the neck even at $D = 0$ mm because of the slower air jet at above $p_{ch} = 30$ kPa. When drawing at above $D = 1$ mm at all chamber pressures, all the fibers formed a neck. Scanning electron micrographs reveal that the nanofiber has a smooth surface that has not been roughened by laser ablation and is without droplets.

Figure 5 shows histograms of the diameters of the nanofibers drawn at four different displacements at $p_{ch} = 10$ and 20 kPa where the nanofibers were obtained, including the average diameter (d_{av}), maximum diameter (d_{max}), minimum diameter (d_{min}), and standard deviation (σ). The nanofibers obtained at $D = 0$ and 3 mm at each chamber pressure have a wider distribution, and the nanofiber obtained at $D = 0$ mm at $p_{ch} = 10$ kPa had the widest distribution ($\sigma = 0.247$ μm). In the case of $D = 0$ mm, the fiber diameter distribution becomes wide (above $\sigma = 0.2$ μm) because the fiber was inhomogeneously drawn by directly irradiating the laser beam top on the fiber at the outlet of the orifice, without the formation of necking as shown in Figure 4. In the case of $D = 3$ mm, since the laser irradiation position moves away from the outlet of the orifice and the drag force becomes feeble, the drawing becomes unstable and the fiber diameter distribution becomes wide. The diameter distribution becomes narrower at $D = 1$ and 2 mm, and that of the nanofiber drawn at $D = 2$ mm at $p_{ch} = 10$ kPa has the narrowest distribution ($\sigma = 0.095$ μm), while its average fiber diameter is 0.543 μm. Thin nanofibers with high uniformity can be obtained by laser irradiation for D in the range of 1–2 mm. This region is approximately the same as that in which high shear and compressive forces were obtained.[28] To produce thinner nanofibers, it is necessary to gradually heat the original fiber by the lower laser power near the beam edge at the position where a higher drag force is generated because the laser power of the beam edge is weaker than that at the center of the beam that has a near-Gaussian profile.

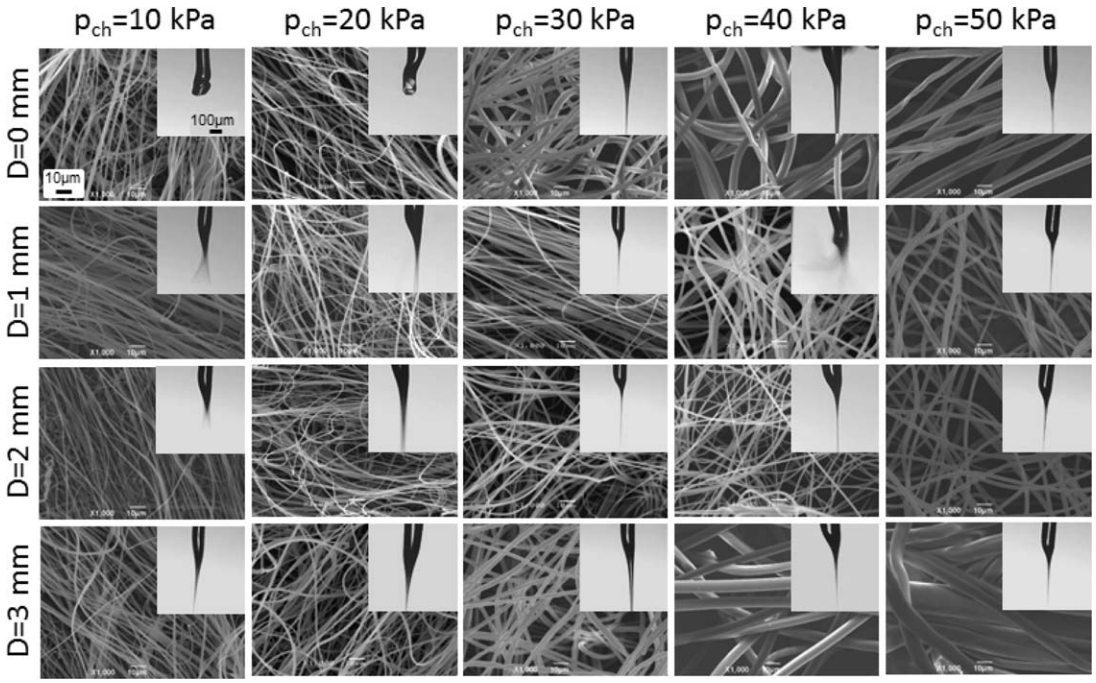

Figure 4. Scanning electron micrographs of the fibers drawn at various chamber pressures (p_{ch}) and displacements (D), including photographs (500×) showing necking formed by the laser heating during the supersonic drawing process.

Figure 6 shows DSC curves for the original fiber and for the fibers obtained by changing the displacement at five different chamber pressures (p_{ch}); Tables I and II list their melting points (T_m) and the degrees of crystallinity (X_c), respectively. The original fiber exhibits a broad single melting peak at 259.3°C. The melting peak can be ascribed to lamellar crystals, which form during the melt spinning to produce the original fiber and DSC measurement. The melting behavior is different depending on the drawing condition used. The fibers obtained at $p_{ch} = 50$ kPa have a single melting peak at about 258°C, the fibers obtained at $p_{ch} = 30$ and 40 kPa have melting peaks at about 257 and traces of a melting peak above 270°C, whereas the fibers obtained at $p_{ch} = 10$ and 20 kPa have two melting peaks at about 257 and above 270°C. The lower melting peak (T_{m1}) is observed at a temperature slightly lower than that of the original fiber, whereas the higher melting peak (T_{m2}) is more 15°C higher than the lower one. The higher melting peaks are observed only in the DSC curves at $p_{ch} = 10$ and 20 kPa where the nanofibers were obtained. Although we have reported the DSC behavior of N66 microfibers obtained by laser heating,[33] the high-temperature peak, as shown in Figure 6, has never been observed previously. The higher melting peak was also observed in the DSC curve of a PET nanofiber as previously reported.[34] The nanofibers produced by CLSD thus show the higher melting peak, which is its unique feature. The existence of crystallites with high melting point is caused by an increase in the intermolecular force in the crystallite, and this increase suggests that the molecular chains are packed closely in the crystallite. The degree of packing of the molecular chain in the crystallite is expressed as the degree of perfection of the crystallite. It is considered that a crystallite with a high melting point is formed by faster plastic deformation induced at supersonic speed that is described subsequently.

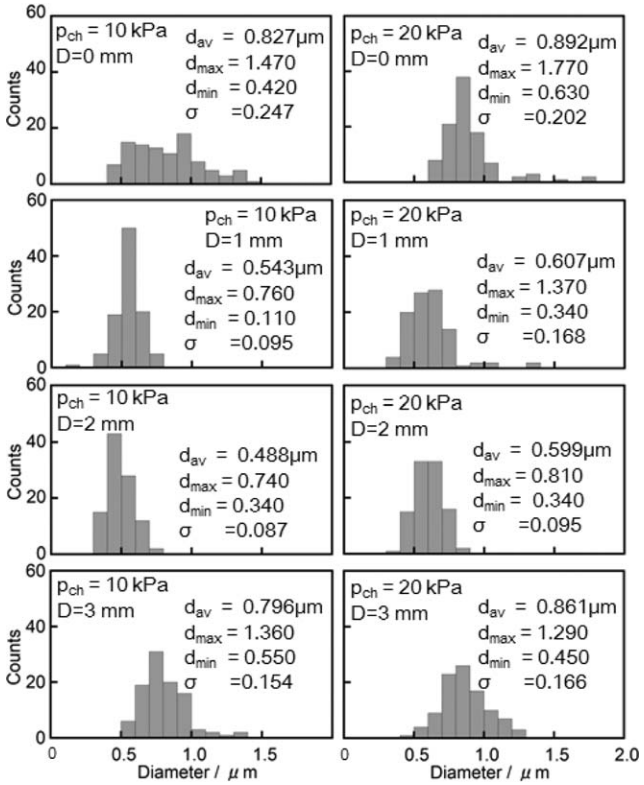

Figure 5. Histograms of the diameters of nanofibers drawn at four different displacements (D) at chamber pressures (p_{ch}) of 10 and 20 kPa.

The degrees of crystallinity (X_{c1} and X_{c2}) were determined from the heats of fusion for the lower and higher melting peaks,

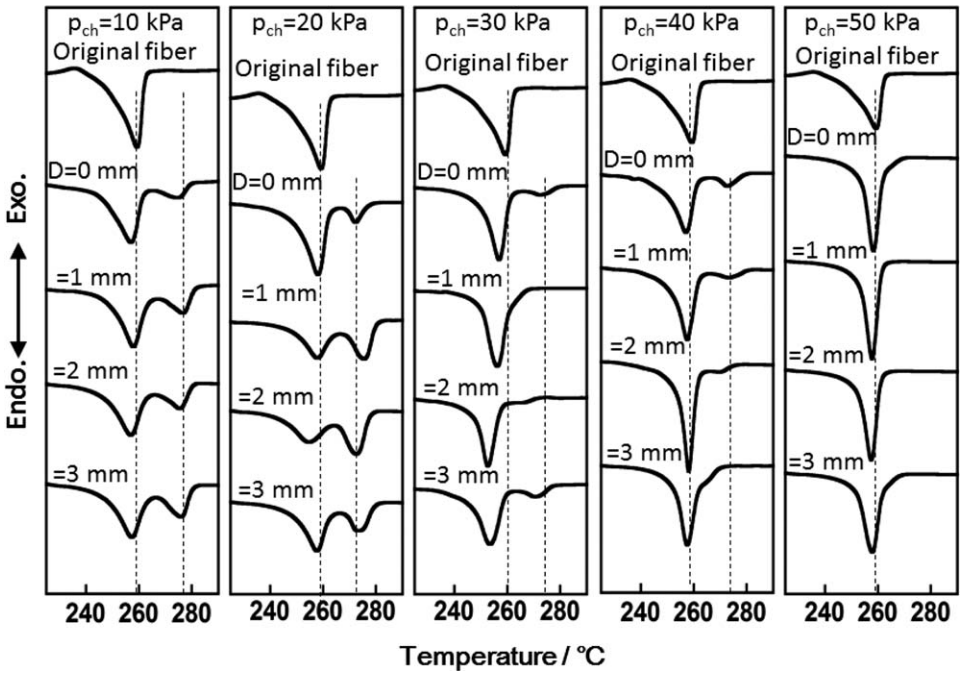

Figure 6. DSC curves of the original fiber and fibers obtained by changing the displacement (D) at five different chamber pressures (p_{ch}).

respectively. The overall degree of crystallinity ($=X_{c1}+X_{c2}$) is highest in fibers produced at $p_{ch}=50$ kPa for all displacements, however, these are not nanofibers. The crystallites with T_{m2} exist only in nanofibers obtained at $p_{ch}=10$ and 20 kPa. The nanofiber formed at $p_{ch}=20$ kPa and $D=2$ mm, which is not the thinnest nanofiber, shows the highest X_{c2} although the whole degree of crystallinity is lower.

Elenga et al.[35] have suggested, from the standpoint of kinetics, that the low-temperature melting peak could be ascribed to extended chain crystals formed by chain unfolding, and that the high-temperature peak corresponds to the untransformed fraction of the lamellar crystals that undergo reorganization during the heating scan. The decrease in the melting point implies that extended chain crystals are formed by chain unfolding during

Table I. Lower Melting Point (T_{m1}) and Higher Melting Point (T_{m2}) for the Original Fiber and the Fibers Obtained by Varying the Displacement (D) at Five Different Chamber Pressures (p_{ch})

	T_{m1}, T_{m2} (°C)				
Sample	$p_{ch}=10$ kPa	$p_{ch}=20$ kPa	$p_{ch}=30$ kPa	$p_{ch}=40$ kPa	$p_{ch}=50$ kPa
Original	259.3, –	259.3, –	259.3, –	259.3, –	259.3, –
$D=0$ mm	257.0, 274.6	258.1, 272.3	256.9, 272.5	257.1, 272.8	258.2, –
$D=1$ mm	257.9, 276.5	257.9, 275.5	256.2, –	257.6, 273.5	258.0, –
$D=2$ mm	256.9, 275.4	254.7, 272.6	252.7, –	258.0, 271.0	257.4, –
$D=3$ mm	257.3, 276.0	257.7, 273.4	253.5, 270.5	257.4, –	257.9, –

Table II. Degrees of Crystallinity (X_{c1} and X_{c2}) Determined From the Heats of Fusion for the Low and High Melting Peaks for the Original Fiber and the Fibers Obtained by Varying the Displacement (D) at Five Different Chamber Pressures (p_{ch})

	X_{c1}, X_{c2} (%)				
Sample	$p_{ch}=10$ kPa	$p_{ch}=20$ kPa	$p_{ch}=30$ kPa	$p_{ch}=40$ kPa	$p_{ch}=50$ kPa
Original	29.8, –	29.8, –	29.8, –	29.8, –	29.8, –
$D=0$ mm	28.5, 5.0	33.0, 4.4	33.8, 2.5	33.1, 3.8	50.2, –
$D=1$ mm	24.6, 8.0	13.2, 12.3	42.5, –	35.6, 2.8	46.5, –
$D=2$ mm	22.9, 7.5	12.5, 14.2	28.0, –	39.2, 1.1	43.8, –
$D=3$ mm	22.5, 9.9	20.1, 9.0	31.3, 3.7	45.6, –	48.4, –

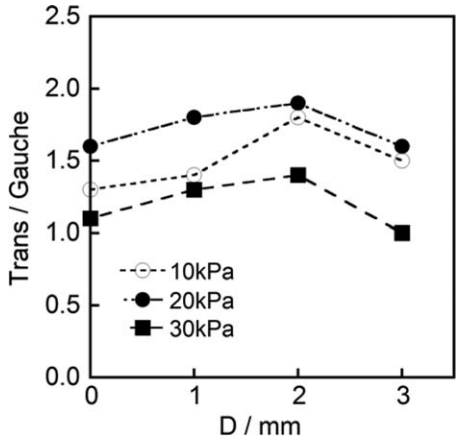

Figure 7. Change in the ratio of the intensity of the *trans* band at 936 cm^{-1} to that of the *gauche* band at 1146 cm^{-1} with displacement (D).

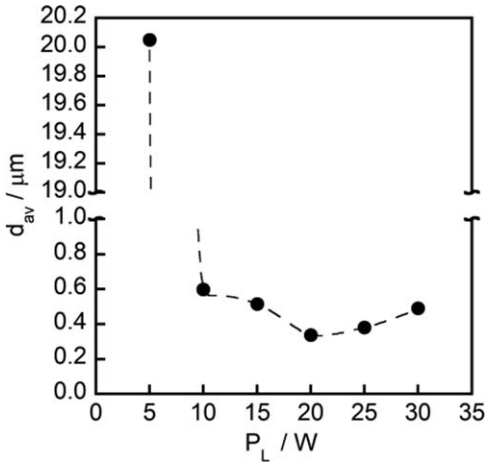

Figure 8. Dependence of the average fiber diameters (d_{av}) on the laser power (P_L).

CLSD. On the other hand, it seems reasonable to consider that the crystallites with T_{m2} are extended chain crystals with a high degree of perfection of the crystallites, because it is difficult to fold back the molecular chains in the supersonic plastic deformation.

To check whether the molecular chains extend during CLSD, a conformational change in the molecular chains in the fibers produced at various displacements and chamber pressures was assessed by FT-IR measurements. Figure 7 shows the change in the ratio of the intensity of the *trans* band at 936 cm^{-1} to that of the *gauche* band at 1146 cm^{-1} for the fibers drawn at $p_{ch} = 10$, 20, and 30 kPa as a function of displacement. The origin of the *trans* and *gauche* bands were tentatively assigned to C–CO stretching and CO twisting.[32] The *trans* conformation can be present in both crystalline and amorphous phases[36]; however, the *gauche* conformation is found only in the amorphous phase.[37]

As the displacement is increased, the *trans*/*gauche* ratio initially increases and then decreases after attaining a maximum diameter at $D = 2$ mm at each chamber pressure. The increase in the amount of the *trans* conformation can be attributed to a morphological change from a folded chain to an extended chain. The CLSD carried out for $D = 2$ mm can thus produce the thinnest nanofiber having extended molecular chains. In other words, the molecular chains are most extended at $D = 2$ mm when the thinner nanofibers were formed.

Laser Power Dependence of Fiber Diameter and Characteristics

Figure 8 shows the dependence of the average fiber diameters (d_{av}) on the laser power (P_L). The chamber pressure, fiber supply speed, and displacement were kept constant at $p_{ch} = 20$ kPa, $S_s = 0.1$ m min^{-1}, and $D = 2$ mm, respectively, during the experiments. As the laser power was increased, the fiber diameter initially decreased and then slightly increased after attaining a minimum diameter at $P_L = 20$ W. The fibers, except for the fiber produced at $P_L = 5$ W, are nanofibers. Thus, laser irradiation at the high power is not necessarily needed to produce the thinner nanofiber.

Figure 9 shows histograms of the nanofiber diameter including average diameter (d_{av}), maximum diameter (d_{max}), minimum diameter (d_{min}), standard deviation (σ), as well photographs (500×) showing the necking formed by laser heating for the fibers obtained at various laser powers. Although all of the fibers are nanofibers with average diameter ranging from 0.3 to 0.6 μm, because of the drawing at optimum chamber pressure and laser irradiation point to produce the nanofibers, the fiber diameter distribution depends on the laser power. The melt viscosity of the fiber becomes lower when irradiated at the lower laser power, and becomes higher when heated at high laser power. A fiber with the lower or higher melt viscosity cannot form stable necking, and the fiber distribution then becomes wider. Irradiation at higher laser power is not necessarily required to produce thinner nanofibers, and the optimum laser power is closely related to the chamber pressure and laser irradiation point. The nanofiber produced at $P_L = 20$ W has a fiber diameter of 0.337 μm, has the narrowest fiber size distribution ($\sigma = 0.061$ μm), and is the thinnest N66 nanofiber in this study.

In melt spinning, the melted polymer ejected from the spinneret expands; this phenomenon is known as the Barus effect.[38] In the case of CLSD performed at $P_L = 10$, 15, and 20 W, all the original fibers were drawn without exhibiting the Barus effect, whereas in CLSD performed at $P_L = 25$ and 30 W, the original fibers were drawn exhibiting the Barus effect. When the original fiber is heated at high laser powers of 25 and 30 W, its melt viscosity decreases to an extreme extent, and the melting region becomes wide. The melted fiber with the lower melt viscosity and wider melting region expands at the end of the neck because the drag force becomes small as the melting position leaves the outlet of orifice.

Another characteristic of the nanofibers produced at $P_L = 25$ and 30 W is that they have transparent areas attributable to optical isotropy at the end of the necking. The appearance of the transparent areas implies that the ends of the necking heated at the higher laser power are amorphous and isotropic. The unstable necking was formed because the melt viscosity in

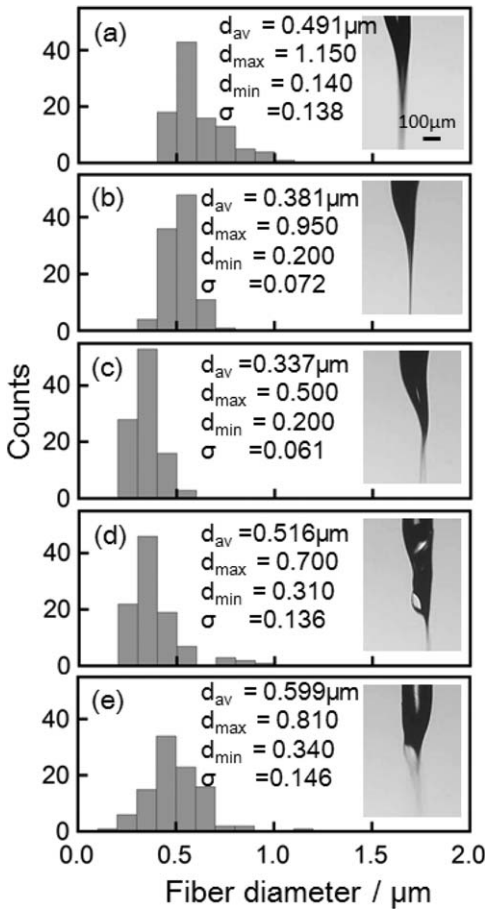

Figure 9. Histograms of the diameter together with photographs (500×) showing the necking formed by laser heating, for fibers obtained at various laser powers (P_L) of (a) $P_L = 10$ W, (b) $P_L = 15$ W, (c) $P_L = 20$ W, (d) $P_L = 25$ W, and (e) $P_L = 30$ W.

the transparent areas is lowest; the formation of unstable necking was confirmed from animated images.

CLSD accompanied by the Barus effect cannot produce thinner nanofibers with a narrow fiber diameter distribution. Thinner nanofibers can be obtained by irradiating the fiber with the laser at an optimum power in the region where a high drag force is generated.

Figure 10 shows DSC curves of the original fiber and the fibers obtained at various laser powers, and Table III lists their low and high melting points (T_{m1} and T_{m2}) and degrees of crystallinity (X_{c1} and X_{c2}) estimated from the low and high melting peaks, respectively. The fiber drawn at $P_L = 5$ W, which has a fiber diameter of 20.1 μm, exhibits a broad single melting peak at 258.5°C. This melting peak can be attributed to crystals formed by flow-induced crystallization during CLSD and that grew during DSC scanning. The fibers obtained at a laser power above 10 W, which have fiber diameters below 1 μm, have two melting peaks at about 257 and above 270°C. The lower melting peak (T_{m1}) is observed at a temperature slightly lower than that of the original fiber, whereas the higher melting peak (T_{m2}) is about 15°C higher than the lower one. The higher melting peaks are observed only in the DSC curves at laser power above

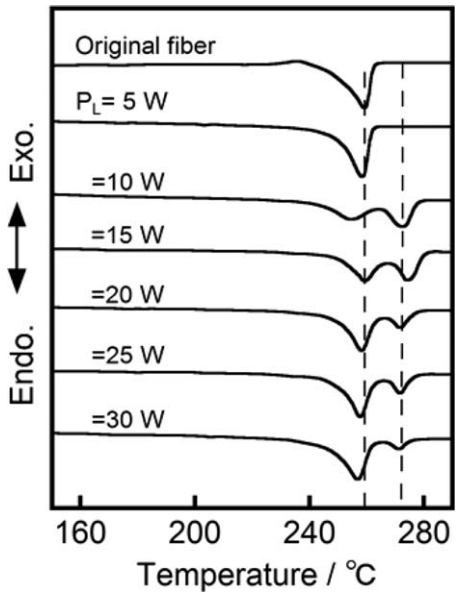

Figure 10. DSC curves of the original fiber and fibers obtained at various laser power values (P_L).

10 W. The X_{c2} value depends on the laser power, and the nanofibers produced at $P_L = 10$ and 15 W show higher X_{c2} and higher T_{m2}. Thus, the thinner the fiber diameter and higher the uniformity, the higher are X_{c2} and T_{m2}. The average fiber diameter, its diameter distribution, and the superstructure show similar tendencies. The appearance of the higher melting peak is thus a rare feature of the nanofibers produced by CLSD.

The moderate melt viscosity necessary to facilitate flow-induced crystallization during CLSD can be obtained at intermediate laser power, and not the high ones. The higher melting peak is caused by an increase in the degree of perfection of the crystallites. The higher the interchain friction, the higher is the degree of perfection of the crystallites.

The drag force to facilitate flow-induced crystallization cannot be obtained because the intermolecular chain friction becomes lower when the high power laser irradiates the fiber, however, the thinner nanofiber cannot be obtained when the interchain

Table III. Lower Melting Point (T_{m1}) and Higher Melting Point (T_{m2}) and Degrees of Crystallinity (X_{c1} and X_{c2}) Determined From the Heats of Fusion of the Low and High Melting Peaks for the Original Fiber and the Fibers Obtained at Various Laser Powers (P_L)

Sample	T_{m1}, T_{m2} (°C)	X_{c1}, X_{c2} (%)
Original	259.3, –	29.8, –
P_L (W)		
5	258.5, –	40.5, –
10	254.7, 272.6	12.5, 14.2
15	259.5, 274.2	14.8, 12.5
20	258.3, 271.7	25.4, 5.5
25	257.8, 271.7	27.2, 6.5
30	257.0, 271.3	33.2, 3.5

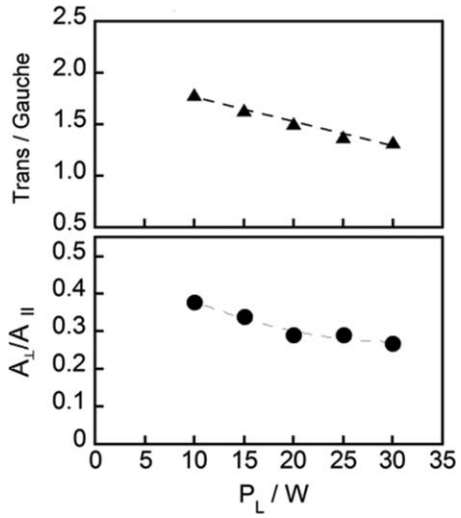

Figure 11. Change in the ratio of the intensity of the *trans* band at 936 cm^{-1} to that of the *gauche* band at 1146 cm^{-1} and the dichroic ratio ($A_\perp/A_{||}$) of the N-H amide band near 1540 cm^{-1} with laser power (P_L).

friction is excessively strong. There are differences in the laser power between the drawing condition to produce the thinner nanofiber and that to facilitate flow-induced crystallization.

Figure 11 shows the change in the *trans*/*gauche* ratio and the dichroic ratio ($A_\perp/A_{||}$) of the N-H amide band[39] at 1540 cm^{-1} as a function of laser power. The *trans*/*gauche* ratio and the dichroic ratio increase as the laser power decreases. The increase in the *trans* conformation and dichroic ratio indicate the morphological change from a folded chain to an extended chain and orientation of the extended chains to the fiber axis. CLSD at lower laser power is effective in producing highly oriented nanofibers. The melt viscosity increases as the laser power decreases, and the increase in the melt viscosity increases intermolecular chain friction. Moderate friction is effective in stretching the molecular chains although it is difficult to extend the molecular chains and to orient molecular chain to the fiber axis when the melt viscosity is too high or too low. The *trans*/*gauche* ratio and the dichroic ratio of the fiber produced at the higher laser power are low because of the lower melt viscosity. The optimum drawing condition to produce the thinner nanofiber and the optimum condition promoting flow-induced orientation and crystallization differ slightly. The IR spectra results imply that moderate melt viscosity due to the intermolecular chain friction promotes chain extension, flow-induced orientation of the amorphous chains, and flow-induced crystallization with the formation of crystal seeds.

To confirm the existence of the oriented crystallites and nuclei formed by the flow-induced crystallization during CLSD, the WAXD measurements were carried out for the nanofibers collected in a bundle and the nanofibers annealed at constant length. Figure 12 shows WAXD patterns for the original fiber and the bundled nanofibers drawn at $p_{ch} = 20$ kPa at various laser powers, and the WAXD patterns including the degree of crystal orientation (π) for the bundled nanofibers annealed at 260°C for 15 min at constant length. The nylon 66 has two known crystal modifications: an α form and a β form,[40] but no reflection due to the β form was observed in their WAXD patterns. The shapes of the diffraction patterns due to (100) reflection and (010)/(110) doublet of the α form in the original fiber were the Debye ring, and the original fiber was isotropic.

No the diffraction patterns were observed in all the nanofibers and they indicated an amorphous halo due to amorphous and isotropic. Although crystallites detectable by X-ray measurement of the nanofibers are not present, it is thought that nuclei are generated in the supersonic drawing process. DSC and FT-IR data of the nanofibers show that the flow-induced crystallization takes place during the supersonic drawing unlike the WAXD measurement. It seems reasonable to consider that the existence of the morphological fine particles such as the nuclei and small crystallites that can hardly be detected by the WAXD measurement exist in the nanofibers. The oriented nuclei and small crystallites formed by superdrawing did not grow up to the crystal size detectable by the WAXD measurement because they were quenched in the low-temperature supersonic jet, which was cooled by adiabatic expansion at the fiber injection orifice.

The WAXD patterns of the annealed nanofibers show the broad arc $\alpha(100)$ reflection and $\alpha(010)/(110)$ doublet due to the oriented crystallites. The arc diffractions on the equator are observed and become sharp as the laser power decreases. To quantitatively determine the degree of crystal orientation (π), the π value was estimated from the half-width (π) of the meridian

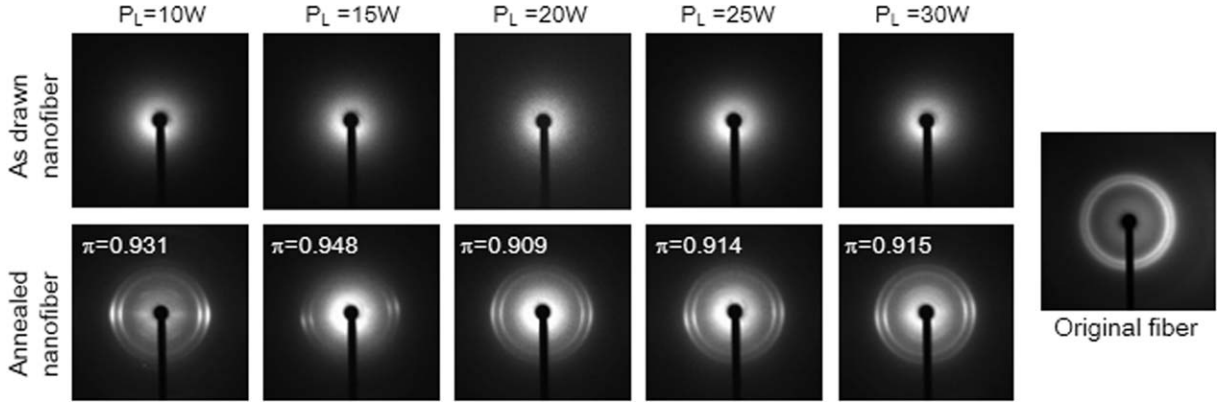

Figure 12. WAXD patterns for the original fiber and the nanofiber drawn at $p_{ch} = 20$ kPa at various laser powers values (P_L), and the WAXD patterns including the degree of crystal orientation (π) for the bundled nanofibers annealed at 260°C for 15 min at constant length.

the α(100) reflection peak. The π values at the low laser power are higher than those at high laser power, the π value at $P_L = 15$ W is 0.948, and the nanofiber drawn at the lower laser power has the highly oriented crystallites. The appearance of the equatorial arc diffractions implied that the oriented nuclei and small crystallites were grown without orientation relaxation by the annealing at constant length. The results of the WAXD measurement verify experimentally that the CO_2 supersonic drawn nanofiber has the crystallites and crystal seeds oriented highly along fiber axis, and that the flow induced crystallization and the formation of the crystal seed occurred during the CO_2 supersonic drawing.

The results of WAXD, DSC, and FT-IR experimentally demonstrate that the nuclei and small crystallites to be undetectable by the WAXD measurement were formed by flow-induced crystallization during CLSD. In our previous articles, it has been reported that PLLA,[24] PET,[34] and iPP[28] nanofibers obtained by CLSD also have the nuclei and small crystallites oriented to the fiber axis.

Fiber Supply Speed Dependence of Fiber Diameter

Figure 13 shows histograms of the diameter, the average (d_{av}), minimum (d_{min}), and maximum (d_{max}) diameters, as well as the standard deviation (σ) together with photographs (500×) showing the necking formed by laser heating for the fibers obtained at various fiber supply speeds (S_s). The chamber pressure, laser power, and displacement between the beam top and the outlet of the orifice were kept constant at $p_{ch} = 20$ kPa, $P_L = 10$ W, and $D = 2$ mm, respectively, in the experiments. Nanofibers were obtained only when the fibers were drawn at $S_s = 0.10$ and 0.15 m min^{-1}. The fibers drawn at $S_s = 0.05$, 0.20, and 0.25 m min^{-1} have an average diameter of about 1 μm and a wider diameter distribution. The melting regions of the fibers drawn at $S_s = 0.20$ and 0.25 m min^{-1} become wider than those of the fibers drawn at slower supply speeds, and longer necking is obtained. The neck at $S_s = 0.25$ m min^{-1} is formed in two stages. The melt viscosity of the fiber heated by the laser at a faster supply speed does not decrease the optimum melt viscosity value needed to effectively superdraw the fiber, because the heating time becomes shorter by faster supply speed. Furthermore, the fiber diameter distribution becomes wide because the drag force becomes feeble and the drawing becomes unstable when the necking point goes away from the outlet of the orifice.

On the other hand, the melt viscosity of the fiber supplied at a slower speed decreases sufficiently and the intermolecular chain friction decreases. This decrease in intermolecular force inhibits stable neck formation in the supersonic jet. Because the drawn fibers swing violently, as shown in Figure 13a, the diameter distribution broadens and the average fiber diameter increases.

In CLSD at $S_s = 0.10$ m min^{-1}, the most stable necking is formed without swaying the drawn fiber, and the thinnest nanofiber with the narrowest fiber diameter distribution is produced.

It is important to know the plastic deformation rate of the fiber drawn in the supersonic jet, but this cannot be measured directly. However, by assuming that the volume of fiber is constant during CLSD, the drawing speed can be approximately estimated as discussed below.

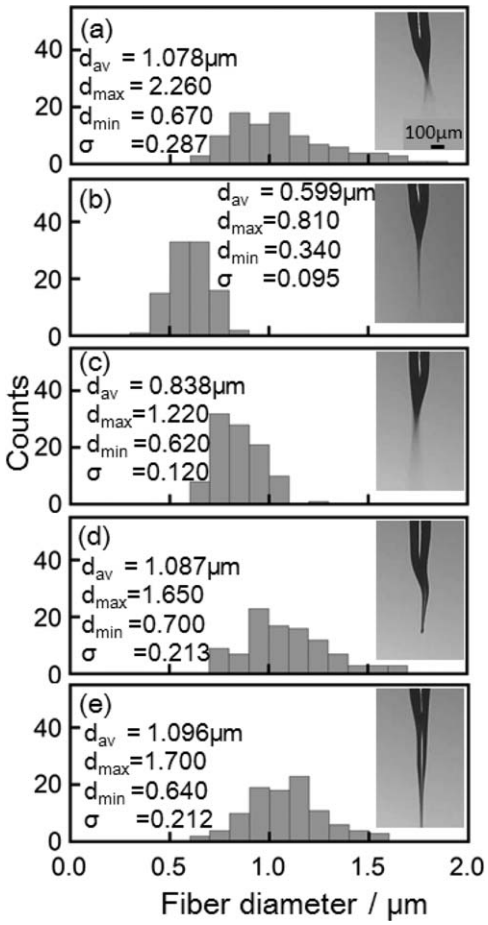

Figure 13. Histograms of the diameter, the average (d_{av}), minimum (d_{min}), and maximum (d_{max}) diameters, together with photographs (500×) showing necking formed by laser heating for the fibers obtained at various fiber supply speeds (S_s) of (a) $S_s = 0.05$ m min^{-1}, (b) $S_s = 0.10$ m min^{-1}, (c) $S_s = 0.15$ m min^{-1}, (d) $S_s = 0.20$ m min^{-1}, and (e) $S_s = 0.25$ m min^{-1}.

When the volumes before and after drawing are assumed to be equal, the following equation applies:

$$\left(\frac{d_o}{2}\right)^2 \pi L = \left(\frac{d_{av}}{2}\right)^2 \pi \ell \tag{3}$$

where d_0 and d_{av} are the diameters of the original fiber and the drawn fiber, and L and ℓ are the length of the supplied original fiber and the drawn fiber, respectively. In *Eq.* 3, L and ℓ are differentiated by the time, and the following equation is obtained:

$$d_o^2 \frac{dL}{dt} = d_{av}^2 \frac{d\ell}{dt} \tag{4}$$

where dL/dt and $d\ell/dt$ are the fiber supply speed (S_s) and drawing speed (S_D). *Equation* 4 can be rewritten as:

$$S_D = \left(\frac{d_0}{d_{av}}\right)^2 S_S. \tag{5}$$

On the other hand, the draw ratio (λ) of the drawn fiber is expressed as[25,26]:

$$\lambda = \frac{\ell}{L} = \left(\frac{d_0}{d_{av}}\right)^2. \quad (6)$$

Therefore, *Eq.* 5 may be written as:

$$S_D = \left(\frac{d_0}{d_{av}}\right)^2 S_S = \lambda S_S. \quad (7)$$

The drawing speed can be calculated easily using *Eq.* 7. The estimated drawing speed of the thinnest nanofiber ($d_{av} = 0.337$ μm) drawn at $S_s = 0.10$ m min^{-1} reaches 486 m s^{-1}, and its draw ratio is 291,664. Thus, extremely large plastic deformation occurs at supersonic speed in CLSD.

CONCLUSIONS

The relationship in CLSD of N66 between the morphology, the superstructure, and the drawing conditions, such as laser power, laser irradiation point, chamber pressure, and fiber supply speed, was investigated. The four drawing factors are closely related, and they need to be optimized to produce thinner nanofibers. The optimum drawing condition to continuously produce the thinnest nanofiber in this study with uniform diameter was clarified by various drawing experiments carried out by varying the four drawing factors. The thinnest N66 nanofiber with a diameter of 0.337 μm and the narrowest diameter distribution was obtained when CLSD was carried out at a laser power of 20 W, chamber pressure of 20 kPa, fiber supply speed of 0.1 m min^{-1}, and displacement of 2 mm. The supersonic drawing speed of the fiber and the draw ratio were estimated from the fiber diameters before and after drawing. The drawing speed estimated for the thinnest nanofiber reached 486 m s^{-1}, and its draw ratio was 291,664. The large plastic deformation at supersonic speed promotes flow-induced orientation and crystallization. The N66 nanofiber has two melting peaks, at about 257 and above 270°C. The nanofiber with the thinnest fiber diameter of 0.337 μm has crystallites with a melting point of 274°C, which is 15°C higher than that of the original fiber. The crystallites are formed by flow-induced crystallization during the instantaneous large deformation obtained at supersonic drawing speed. The appearance of crystallites with the higher melting point suggests that the molecular chains are packed closely in the crystallite. Crystallites with a high degree of crystal perfection are produced by the superflow induced crystallization during CLSD, and their appearance is the rare and unique feature of nanofibers produced by CLSD. Thus, CLSD cannot only produce N66 nanofibers without using any solvent and removing the second component but can also improve its thermal resistance by only physical treatment without modification of the molecular structure.

REFERENCES

1. Yeo, Y.; Jeon, D.; Kim, C.; Choi, S.; Cho, K.; Lee, Y.; Kim, C. *J. Biomed. Mater. Res.* **2005**, *72B*, 86.
2. Lee, K.; Givens, S.; Chase, D. B.; Rabolt, J. F. *Polymer* **2006**, *47*, 8013.
3. Zong, X.; Kim, K.; Fang, D.; Ran, S.; Hsiao, B. S.; Chu, B. *Polymer* **2002**, *43*, 4403.
4. Meng, J.; Song, L.; Meng, J.; Kong, H.; Zhu, G.; Wang, C.; Xu, L.; Xie, S.; Xu, H. *J. Biomed. Mater. Res.* **2006**, *79A*, 298.
5. You, Y.; Min, B. M.; Lee, S. J.; Lee, T. S.; Park, W. H. *J. Appl. Polym. Sci.* **2005**, *95*, 193.
6. Kim, B. S.; Mooney, D. J. *J. Biomed. Mater. Res.* **1998**, *41*, 322.
7. Higgins, S. P.; Solan, A. K.; Niklason, L. E. *J. Biomed. Mater. Res.* **2003**, *67A*, 295.
8. Gao, J.; Niklason, L.; Langer, R. *J. Biomed. Mater. Res.* **1998**, *42*, 417.
9. Eugene, D. B.; Todd, A. T.; David, G. S.; Gary, E. W.; Gary, L. B. *J. Biomed. Mater. Res.* **2004**, *71B*, 144.
10. Ding, B.; Kimura, E.; Sato, T.; Fujita, S.; Shiratori, S. *Polymer* **2004**, *45*, 1895.
11. Gupta, P.; Wilkes, G. L. *Polymer* **2003**, *44*, 6353.
12. Ayutsede, J.; Gandhi, M.; Sukigara, S.; Micklus, M.; Chen, H. E.; Ko, F. *Polymer* **2005**, *46*, 1625.
13. Fong, H. *Polymer* **2004**, *45*, 2427.
14. Kim, J. S.; Reneker, D. H. *Polym. Eng. Sci.* **1999**, *38*, 849.
15. Deitzel, J. M.; Kleinmeyer, J.; Harris, D.; Tan, B. N. C. *Polymer* **2001**, *42*, 261.
16. Huang, C.; Chen, S.; Reneker, D. H.; Lai, C.; Hou, H. *Adv. Mater.* **2006**, *18*, 668.
17. Pedicini, A.; Farris, R. *J. Polym.* **2003**, *44*, 6857.
18. Varabhas, J. S.; Chase, G. G.; Reneker, D. H. *Polymer* **2008**, *49*, 4226.
19. Zhou, H.; Green, T. B.; Joo, Y. *Polymer* **2006**, *47*, 7497.
20. Dalton, P. D.; Grafahrend, D.; Klinkhammer, K.; Klee, D.; Möller, M. *Polymer* **2007**, *48*, 6823.
21. Lyons, J.; Li, C.; Ko, F. *Polymer* **2004**, *45*, 7597.
22. Ellison, C. J.; Phatak, A.; Giles, D. W.; Macosko, C. W.; Bates, F. S. *Polymer* **2007**, *48*, 3306.
23. Borkar, S.; Gu, B.; Dirmyer, M.; Delicado, R.; Sen, A. N.; Jackson, B. R.; Badding, J. V. *Polymer* **2006**, *47*, 8337.
24. Suzuki, A.; Aoki, K. *Eur. Polym. J.* **2008**, *44*, 2499.
25. Suzuki, A.; Tanizawa, K. *Poymer* **2009**, *50*, 913.
26. Suzuki, A.; Yamada, Y. *J. Appl. Polym. Sci.* **2010**, *116*, 1913.
27. Suzuki, A.; Shimizu, R. *Appl. Polym. Sci.* **2011**, *121*, 3078.
28. Suzuki, A.; Arino, K. *Eur. Polym. J.* **2012**, *48*, 1169.
29. Fukuhara, K.; Yamada, T.; Suzuki, A. *Ind. Eng. Chem. Res.* **2012**, *51*, 10117.
30. Suzuki, A.; Hayashi, H.; *eXPRESS Polym. Lett.* **2013**, *7*, 519.
31. Zussman, E.; Burman, M.; Yarin, A. L.; Khalfun, R.; Cohen, Y. *J. Polym. Sci. Part B: Polym. Phys.* **2006**, *44*, 1482.
32. Quintanilla, L.; Rodriguez-Cabello, J. C.; Pastor, J. M. *Polymer* **1994**, *35*, 2321.

33. Suzuki, A.; Hasegawa, T. *Appl. Polym. Sci.* **2006**, *99*, 802.
34. Suzuki, A.; Arino, K. *Polymer* **2010**, *51*, 1830.
35. Elenga, R.; Seguela, R.; Rietsch, F. *Polymer* **1991**, *32*, 1975.
36. Pearce, R.; Cole, K. C.; Ajji, A.; Dumolin, M. M. *Polym. Eng. Sci.* **1997**, *1795*.
37. Ajji, A.; Cole, K. C.; Dumolin, M. M.; Ward, I. M. *Polym. Eng. Sci.* **1997**, *1801*.
38. Ishibashi, T. *J. Appl. Polym. Sci.* **1974**, *18*, 2427.
39. Shao, H.-l.; Umemoto, S.; Kikutani, T.; Okui, N. *Polymer* **1997**, *38*, 459.
40. Bunn, C. W.; Gardner, E. V. *Proc. R. Soc.* **1947**, *189*, 39.